High-Power and High-Energy-Density Flexible Pseudocapacitor Electrodes Made from Porous CuO Nanobelts and Single-Walled Carbon Nanotubes

Xiaojun Zhang,[†,‡] Wenhui Shi,[†] Jixin Zhu,[†] Daniel Julian Kharistal,[†] Weiyun Zhao,[†] Boor Singh Lalia,[§] Huey Hoon Hng,[†,*] and Qingyu Yan[†,§,*]

[†]School of Materials Science and Engineering, Nanyang Technological University, Singapore 639798, Singapore, [‡]College of Chemistry and Materials Science, Anhui Normal University, Wuhu 241000, P. R. China, and [§]Energy Research Institute@NTU, Nanyang Technological University, Singapore 637459, Singapore

ABSTRACT We report a simple wet-chemical process to prepare porous CuO nanobelts (NBs) with high surface area and small crystal grains. These CuO NBs were mixed with carbon nanotubes in an appropriate ratio to fabricate pseudocapacitor electrodes with stable cycling performances, which showed a series of high energy densities at different power densities, for example, 130.2, 92, 44, 25, and 20.8 W h kg^{-1} at power densities of 1.25, 6.25, 25, and 50 k Wh kg^{-1}, respectively. CuO-on-single-walled carbon nanotube (SWCNT) flexible hybrid electrodes were also fabricated using the SWCNT films as current collectors. These flexible electrodes showed much higher specific capacitance than that of electrodes made of pure SWCNTs and exhibited more stable cycling performance, for example, effective specific capacitances of >62 F g^{-1} for the hybrid electrodes after 1000 cycles in 1 M LiPF6/EC:DEC at a current density of 5 A g^{-1} and specific capacitance of only 23.6 F g^{-1} for pure SWCNT electrodes under the same testing condition.

KEYWORDS: CuO · porous nanobelts · pseudocapacitor electrodes · power density · energy density · flexible electrode

The development of alternative energy storage/conversion devices has attracted great attention due to increasing concern of environmental issues and the depletion of fossil fuels.[1−3] Pseudocapacitors,[4,5] as an intermediate system between dielectric capacitors and batteries, have attracted much interest owing to their higher power densities than that of secondary batteries, and higher energy density as compared to traditional electric double-layer capacitors. The pseudocapacitors normally combine the nonfaradic electrostatic charge storage process[6,7] with redox reactions[8−11] to achieve high capacitances.

It is important for pseudocapacitors to attain high specific surface area, high electrical conductivity, and a fast cation diffusion process to achieve high power densities and energy densities. Ruthenium oxides and hydroxides have been previously demonstrated to show very high pseudo-charge-capacitance, for example, 1300 F g^{-1}.[12,13] However, the high cost limits their applications. Other transition metal oxides,[14−23] such as NiO, Co_3O_4, MnO_2, and VO_x, were later considered and well studied. Among these metal oxides, CuO can be a promising candidate due to its low cost, and it is chemically stable and environmental-friendly. Besides being useful as catalysts[24] and biosensors,[25,26] CuO nanostructures have also been tested as Li ion battery anodes and showed high Li-ion storage capacities,[27] which suggests that CuO can offer high-charge storage capacity through a redox reaction. However, to our best knowledge, little work has been carried out on the application of CuO as supercapacitor/pseudocapacitor electrodes because of their low electrical conductivity and unstable cycling performances.[28,29] The poor capacitance retention upon cycling is mainly due to the destruction of the crystal structure of CuO during the ion insertion−extraction process. Controlled nanostructuring of the material may help to solve this problem. It has been demonstrated that improved cyclability can be achieved for CuO as Li ion battery anodes through synthesis of unique nanostructures, for example, urchin-like CuO nanoparticles showed much better cycling stability as compared to cubic CuO nanoparticles.[27]

Herein, we report the synthesis of porous CuO nanobelts that can be used to make flexible electrodes with promising charge storage performances. These porous CuO nanobelts had a large surface area (128 m^2 g^{-1}) and were polycrystalline with extremely small crystal grains (*e.g.*, 3−5 nm). This led to their high capacitances and stable cycling performances when tested as

* Address correspondence to alexyan@ntu.edu.sg, ashhhng@ntu.edu.sg.

Received for review November 12, 2010 and accepted February 10, 2011.

Published online February 18, 2011
10.1021/nn1030719

pseudocapacitor electrodes in 1 M $LiPF_6$/EC:DEC, for example, 128 F g^{-1} after 1000 cycles at a current density of 1 A g^{-1} in the potential range of 0−2.5 V *vs* SCE. We further prepared CuO-on-single-walled carbon nanotube (SWCNT) flexible electrodes using SWCNT films as current collectors. The average specific capacitances of the CuO-on-SWCNT electrodes, calculated on the basis of the total mass of the CuO nanobelts and SWCNT current collectors, were much higher than that of electrodes made of pure SWCNTs. Effective specific capacitances of >62 F g^{-1} for the CuO-on-SWCNT electrodes were obtained after 1000 cycles in 1 M $LiPF_6$/EC:DEC at a current density of 5 A g^{-1} in the potential range of 0−2.5 V *vs* SCE, while the electrodes made of pure SWCNTs showed specific capacitance of only 23.6 F g^{-1} under the same testing condition.

RESULTS AND DISCUSSION

The synthesis of the porous CuO nanobelts started from the mixing of $Cu(NO_3)_2$ and ammonia in distilled water as described in the Methods section, which led to the formation of blue precipitates. Transmission electron microscopy (TEM) images of the blue precipitates (see Supporting Information Figure S1a-b) revealed 1D belt structures with lengths in the range of 2−10 μm. The width of the belts was 100−150 nm. The X-ray diffraction (XRD) pattern (see Supporting Information Figure S2) revealed that the blue intermediate products were orthorhombic $Cu(OH)_2$ (JCPDS Card No. 80-0656, lattice constant a = 0.2947, b = 1.059, and c = 0.5256 nm) with no detectable impurity phase. Here, the peaks positioned at 23.8, 34.1, 39.8, and 53.4 degree corresponded to (021), (002), (130), and (132) of $Cu(OH)_2$, respectively. The blue precipitates in distilled water were sealed in autoclaves and heated at 60 °C for 4 h, which resulted in the final brownish products. The TEM image (see Figure 1a) showed that the brownish products were also belt-shape with smaller widths and lengths, 5−10 nm and 1−3 μm, respectively. The selected area electron diffraction (SAED) pattern (see Figure 1c) showed that these nanobelts obtained from the hydrothermal process at 60 °C were monoclinic CuO (JCPDS Card No. 41-0254, lattice constant a = 0.4685, b = 0.3423, and c = 0.5132 nm). The high resolution TEM (HRTEM) image (see Figure 1b and Supporting Information Figure S3) indicated that these CuO nanobelts were polycrystalline with crystal size in the range of 3−5 nm, and there were nanopores of 2−5 nm in the CuO nanobelts. As some of the CuO nanobelts were rolled up to provide the side view of the nanobelts (see the HRTEM images in Supporting Information Figure S4), the thickness of the nanobelts could be estimated to be 2−5 nm. The transition from $Cu(OH)_2$ to CuO through this hydrothermal reaction was also revealed by the XRD patterns (see Supporting Information Figure S2), which correspond to samples reacted in the autoclaves for different duration. It showed that there were both $Cu(OH)_2$ and CuO phases in samples reacted for 2 and 3 h. For sample after 4 h reaction, only diffraction peaks from CuO were observed, which indicated that $Cu(OH)_2$ had transformed to CuO. Here, the peaks positioned 32.5, 35.4, 38.7, and 48.7 deg corresponded to (110), (002), (111), and (020) of CuO, respectively. TEM images (see Supporting Information Figures S4a−f) of samples obtained with different reaction times showed that the width of the nanobelts decreased from 80 to 150 nm to 5−10 nm upon increasing the reaction duration from 1 to 3 h. High magnification TEM images revealed that pores of 3−5 nm were generated in these intermediate products while accumulation of the pores led to fracture of the nanobelts (see Supporting Information Figure S4e,f and Figure S5) The proposed transition mechanism from $Cu(OH)_2$ to CuO was attributed to the dehydration and recrystallization of $Cu(OH)_2$ at elevated temperatures.[30]

The specific surface area of the CuO nanobelts was investigated by BET techniques. The N_2 gas adsorption−desorption isotherm of the CuO nanobelts (see Supporting Information Figure S6a) reveals a hysteresis loop that was characteristic of porous materials. The specific area was determined to be 128 m^2 g^{-1}. Although the pore size distribution plot (see Supporting Information insert in Figure S6a) could be obtained on the basis of the analysis of the desorption branch data, we were not able to draw a plausible conclusion on the pore size distribution in these CuO samples as

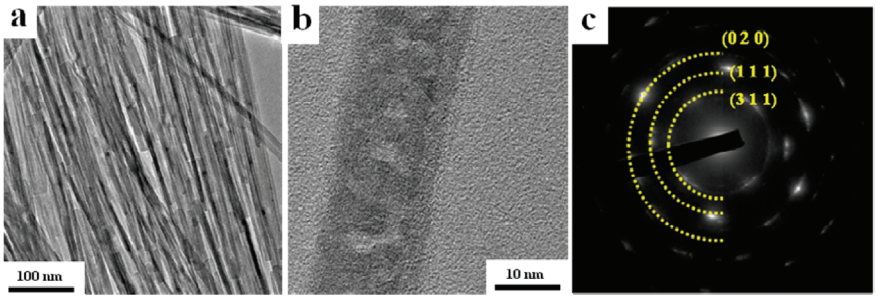

Figure 1. (a) TEM and (b) HRTEM images of as-prepared CuO nanobelts with diameter of 5−10 nm and lengths up to several micrometers; (c) SAED pattern of the CuO nanobelt shown in panel b. The enlarged image of panel b is provided in Supporting Information Figure S3.

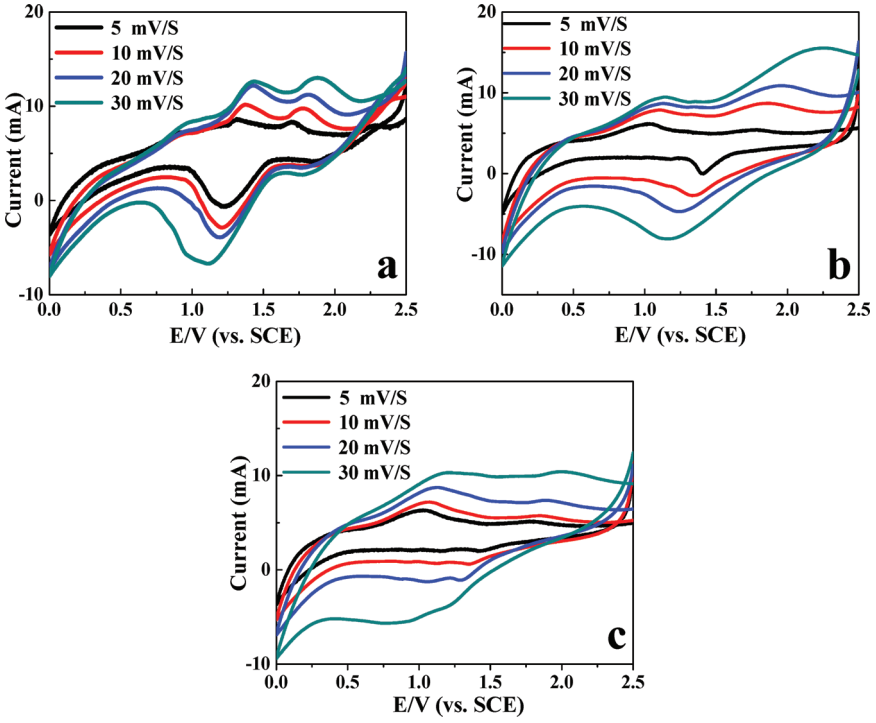

Figure 2. Cycling voltammogram curves of different electrodes: (a) pure CuO electrode, (b) CuO nanobelts mixed with SWCNTs (9:1 weight ratio) electrode, and (c) CuO nanobelts mixed with carbon black (CB) and the PVDF binder electrode in 1.0 M LiPF6/EC:DEC with different scan rates.

other factors might also be reflected in the physisorption isotherms, for example, the interbelt space might also be counted.

To evaluate the charge storage capacity of these porous CuO nanobelts, several electrodes on Cu foils were made, such as CuO nanobelts mixed with SWCNTs (9:1 weight ratio, named as CuO/CNTs electrode), pure CuO nanobelts (named as CuO electrode), and CuO nanobelts mixed with carbon black and the PVDF binder (9:1:1 weight ratio, named as CuO/CB electrode). The SEM images (see Supporting Information Figure S7) of all three types of electrodes indicated that CuO nanobelts were uniformly distributed on the Cu foils. For CuO/CB electrodes, the CuO nanobelts (see Figure Supporting Information S7a,b) and carbon black were uniformly mixed (see Supporting Information Figure S7c,d). However, for CuO/CNTs electrodes, we could not clearly distinguish the difference between the CuO nanobelts and SWCNTs in the SEM image (see Supporting Information Figure S7e,f). The specific surface area and pore size distribution of CuO/CNT and CuO/CB electrodes was also evaluated by BET measurements. The results were very similar to that of pure CuO nanobelts (see Supporting Information Figure S6b,c). These electrodes were then subjected to cyclic voltammograms (CV) and chronopotentiometric measurements in 1.0 M $LiPF_6$/EC:DEC in the potential range of 0−2.5 V *vs* SCE. The CV curves of pure CuO electrodes at different scan rates (see Figure 2a) show clear pairs of cathodic and anodic peaks, which correspond to the redox process between Cu^{2+} and Cu^0.[31,32] The addition of conductive phases such SWCNTs or carbon black caused the cathodic and anodic peaks to become less obvious (see Figure 2b and 2c). The specific capacitances, C_s, of the CuO nanobelts-based electrodes were calculated from the galvanostatic discharge curves (see Figure 2a) using the following equation:[33]

$$C_s = \frac{i}{-\frac{\Delta V}{\Delta t}m} = \frac{i}{-\text{slope} \times m}$$

where i is the current applied, $\Delta V/\Delta t$ is the slope of the discharge curve after the iR drop, and m is the mass of the sample on one electrode. The CuO electrode depicted a high C_s value of 130 F g^{-1} at a current density of 1 A g^{-1}, which was attributed to its high surface area and small crystal grain size. The CuO/CNT electrode depicted an even higher C_s value of 150 F g^{-1} at 1 A g^{-1}, which was possibly due to the SWCNTs that served as highly conductive scaffolds to allow the effective charge transfer and cation diffusion between the electrodes and electrolyte. The CuO/CB electrode showed a slightly lower capacitance of 127 F g^{-1} at 1 A g^{-1}. Here, it is worth pointing out that the mass of the PVDF binder was included in the total mass of the CuO/CB electrodes during the calculation of the specific capacitances, which led to a lower specific capacitance. Here, the higher specific capacitance obtained in the CuO/CNTs electrodes indicated that the combination of the non-Faradic and Faradic charge storage processes could effectively increase the effective specific capacitance of the

pseudocapacitor electrodes, which was similar to the bind-free Li-ion battery made from SWCNTs and Fe_3O_4.[34]

The cyclability of these CuO nanobelts based electrodes were tested by continuous charge/discharge measurements over 1000 cycles (see Figure 3) at a current density of 1 A g^{-1} within a voltage range of 0−2.5 V. A slight increase in the capacitances was observed during the first 50 cycles for the CuO/CNTs and CuO/CB electrodes, which was attributed to the activation process[35] allowing the trapped cations in the CuO crystal lattice to gradually diffuse out. Such increase in the capacitance during cycling test was not detectable for the pure CuO electrodes. This is possibly due to the decrease in capacitance as the electrodes degrade during the cycling charge/discharge processes, which obscured the activation effect. The CuO/CNTs electrodes exhibited the best cycling stability among the three types of electrodes tested, for example, there was only 10% drop of the specific capacitance after 1000 charge/discharge processes as compared to 41% for pure CuO electrodes and 18% for CuO/CB electrodes. The specific capacitance of the CuO/CNTs electrode retained at 128 F g^{-1} after 1000 charge/discharge cycles as compared to 101 F g^{-1} and 73 F g^{-1} for CuO/CB and pure CuO electrodes, respectively. The SEM image of the CuO/CNTs electrode after 1000 charge/discharge cycles (see Supporting Information Figure S8a,b) revealed that the sample still remained as open networks with large surface area formed by the entangled 1D nanostructures. No obvious deformation of the 1D nanostructures was observed, which was consistent with their stable cycling performance upon charge/discharge.

The charge and ion transfer characteristics of all three types of electrodes were further investigated by electrochemical impedance spectroscopy (EIS). The Nyquist diagrams for the three types of electrodes are presented in Supporting Information, Figure S9. The Nyquist diagrams for the three electrodes consisted of approximate semicircles at high frequencies and lines at low frequencies. The semicircle is related to the Faradaic reactions and its diameter represents the interfacial charge-transfer resistance (usually termed as Faradaic resistance). The slope of the lines at low frequency is related to the diffusion resistance of the electrolyte in the electrode pores. The Nyquist diagrams of the CuO/CNTs electrode before and after 1000 charge−discharge cycles showed semicircles with smaller diameters than those of the CuO/CB and pure CuO electrodes, which indicates that the ion transfer was more effective in the CuO/CNTs electrodes. The high frequency intercept of the semicircle with the real axis gives the bulk resistance of the solution and the active material. The addition of CNT and CB in CuO results in the decrease in bulk resistance and hence improve the electrochemical performance of the pseudocapacitor. Meanwhile, the slopes of the straight lines at low frequency for the CuO/CNTs electrode before and after 1000 charge−discharge cycles were larger than that of the CuO/CB and pure CuO electrodes. These showed that the reaction and diffusion resistances for the CuO/CNTs electrodes were smaller than that of the CuO/CB and pure CuO electrodes, which was consistent with the better pseudocapacitor performance of the CuO/CNTs electrode.

The galvanostatic charge/discharge curves of the CuO/CNTs electrode were also tested under different current densities (see Figure 4). These results were used to estimate the energy densities of the CuO/CNTs electrode at different power densities, which were important parameters to evaluate the electrochemical performance of the electrochemical cells. The energy densities and corresponding power densities were calculated from the following equations,[36,37] and the results are listed in Table 1:

$$P = \frac{V^2}{4RM}$$

$$E = \frac{1}{2}CV^2 = \frac{1}{8}MC_{SP}V^2$$

where V is the applied voltage, R is the equivalent series resistance (ESR), M is the total mass of the electrodes, and C is the total capacitance of electrode ($C = C_{sp}M/4$).[38]

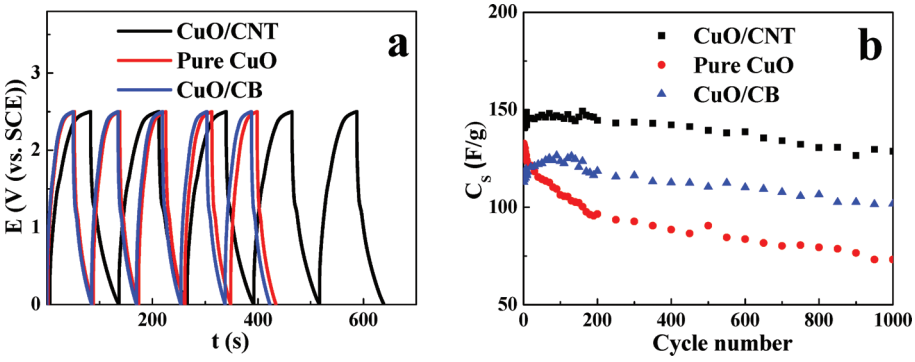

Figure 3. (a) Galvanostatic charge/discharge curves measured with a current density of 1 A g^{-1} for different electrodes; (b) cycling performance for different electrodes at a current density of 1 A g^{-1} in 1.0 M LiPF6/EC:DEC.

The specific capacitances of the CuO/NTs electrode obtained from the galvanostatic curves were 150, 106, 51, and 24 F g^{-1} at current densities of 1, 5, 20, and 40 A g^{-1}, respectively. These values corresponded to a series of energy densities of 130.2, 92.0, 44.0, and 20.8 W h kg^{-1} at different power densities of 1.25, 6.25, 25, and 50 kW kg^{-1}, respectively. Such high energy densities and power densities are better than that of supercapacitor electrodes recently reported;[39−41] for example, the energy density of 3D periodic hierarchical porous graphitic carbon is 5.3 W h kg^{-1} at a power density of 25 kW kg^{-1}, and the energy density of SnO_2/MnO_2 composites is 35.4 W h kg^{-1} at a power density of 25 kW kg^{-1}. These results suggested that the porous CuO nanobelts could be considered as promising electrode materials for pesudocapacitor applications.

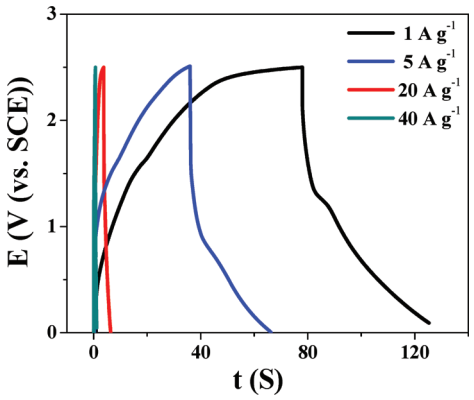

Figure 4. Galvanostatic charge/discharge curves measured with different current density for CuO nanobelts mixed with SWCNTs (9:1 weight ratio) electrode.

TABLE 1. Specific Capacitance, Power Density, And Energy Density of CuO/CNT Electrodes at Different Current Densities

current density (A g^{-1})	40	20	5	1
specific capacitance (F g^{-1})	24	51	106	150
power density (kW kg^{-1})	50	25	6	1.25
energy density (kW kg^{-1})	20.8	44	92	130.2

We further fabricated flexible electrodes by depositing the mixture of CuO nanobelts and SWCNTs (weight ratio 9:1) as network films onto pure SWCNT films without the addition of any binders (see Figure 5a). The thickness of the CuO/CNTs network films was about 100 μm and the thickness of the SWCNT films was about 50 μm. Here, the pure SWCNT films act as the current collector because of their low internal resistance. The SWCNT films should also contribute to the total capacitance of the electrodes through electric double layer charge storage. The flexible electrodes were quite robust upon repeated bending (see Figure 5b). The SEM image of the electrode showed that uniformly mixed 1D nanostructures formed the network films (see Figure 5c). We tested the galvanostatic charge/discharge curves (see Figure 5d) of the CuO-on-SWCNT flexible electrode (CuO/CNTs on SWCNT current collector) at 5 A g^{-1} in 1.0 M $LiPF_6$/EC:DEC within the potential range of 0−2.5 V *vs* SCE. The calculated effective specific capacitance of the whole flexible electrode (including the mass of the

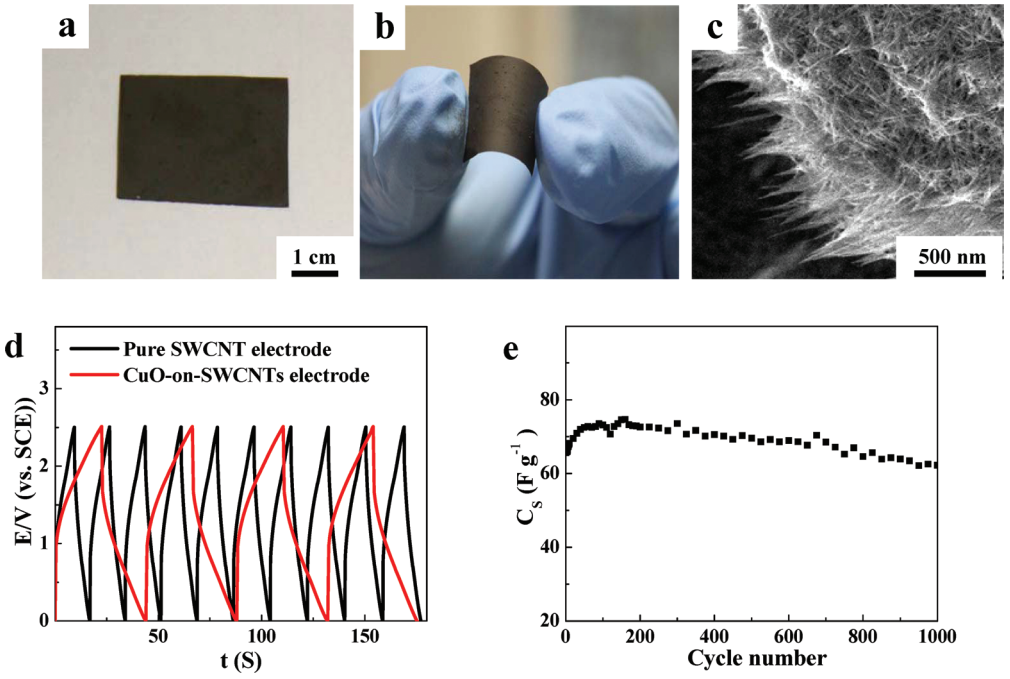

Figure 5. (a,b) Optical image of CuO nanobelts-based two-layered SWCNTs@CuO nanobelts mixed with SWCNTs (9:1 weight ratio) electrode; (c) the edge of SWCNTs@CuO nanobelts mixed with SWCNTs electrode; (d) Galvanostatic charge/discharge curves measured with a current density of 5 A g^{-1} for different electrodes. (e) Cycling performance for SWCNTs@CuO nanobelts mixed with SWCNTs electrode at a current density of 5 A g^{-1} in 1.0 M LiPF6/EC:DEC.

SWCNT current collector) was 75.7 F g^{-1}. For comparison, the specific capacitance of the pure SWCNT electrodes was also obtained from their galvanostatic curves (see Figure 5d) measured under the same condition. The specific capacitance of the pure SWCNT electrodes was only 23.6 F g^{-1} in 1.0 M $LiPF_6$/EC:DEC, which is similar to previously reported value.[42] The cyclability of these CuO-on-SWCNT flexible electrodes was also investigated by continuous charge/discharge measurements over 1000 cycles (see Figure 5e) at a current density of 5 A g^{-1} within the voltage window of 0 to 2.5 V. The specific capacitance only dropped a little to 62.4 F g^{-1} after 1000 cycles, which indicates their stable cycling performances.

CONCLUSIONS

We have used a simple chemical method to synthesize porous CuO nanobelts with large specific surface area and small grain size. These porous CuO nanobelts were further tested as pseudocapacitor electrode materials, which were found to exhibit superior performance in terms of specific capacitance, cyclability, energy density, and power density. We further fabricated flexible CuO-on-SWCNT electrodes using pure SWCNT films as current collectors. These CuO-on-SWCNT flexible electrodes also showed stable cycling performances upon repeated charging/discharging process and had much higher specific capacitances than that of pure SWCNT electrodes under the same testing condition. These results indicated that such porous CuO nanobelts could be considered as promising electrode materials for pseudocapacitor applications, especially for developing completely flexible pseudocapacitor using solid polymer electrolytes.

METHODS

Chemicals. $Cu(NO_3)_3 \cdot 6H_2O$, ethanol, and $NH_3 \cdot H_2O$ were purchased from Sigma Chemical Corp and 1.0 M $LiPF_6$ in 1:1 w/w ethylene carbonate/diethyl carbonate ($LiPF_6$/EC:DEC) was purchased from Ferro Corporation. All chemicals were used as received without any further purification. Millipore water was used in all experiments.

Synthesis of CuO Nanobelts. In a typical synthesis process, 0.5 g of $Cu(NO_3)_2$ was dissolved into 100 mL of distilled water. Then, 20 mL of ammonia (0.3 M) solution was added to the $Cu(NO_3)_2$ solution under constant stirring. After stirring for 15 min, blue $Cu(OH)_2$ precipitates formed, which were then sealed in an autoclave and heated at 60 °C for 4 h. Finally, the brownish products were cleaned by repeated washing with ethanol/distilled water and centrifuging.

Characterization. X-ray powder diffraction (XRD) patterns were recorded on a Shimadzu XRD-6000 X-ray diffractometer at a scan rate of 0.05 deg/s using Cu Kα radiation. The size and morphology of the samples were characterized using a field-emission SEM (JEOL JSM6335) operating at 10 kV. TEM and SAED measurements were carried out in a JEOL 2010 system operating at 200 kV. Nitrogen adsorption/desorption isotherms were measured on a Micromeritics TriStar 3000 porosimeter (mesoporous characterization) and Micromeritics ASAP 2020 (microporous characterization) at 77 K. All samples were outgassed at 60 °C for 6 h under vacuum before measurement. The specific surface areas were calculated using the Brunauer–Emmet–Teller (BET) methods. Pore size distribution (PSD) plots were obtained by Barrett–Joyner–Halenda (BJH) method using desorption branch and cylindrical pore model. Micropore size distribution (MPSD) plots were obtained by Horvath and Kawazoe (HK) method using cylindrical pore model.

Electrochemical Tests. The CuO nanobelts were mixed with SWNTs with a weight ratio of 9:1 in ethanol solution without adding any binder. The solution was sprayed onto Cu foils dried at 40 °C for 2 h under vacuum to form pseudocapacitor electrodes (named as CuO/CNTs electrode). Pure CuO nanobelts were also sprayed onto Cu foils by a similar process to fabricate CuO electrodes. The as-prepared three electrodes have similar configuration. The thickness of each electrode is about 100 μm, the size of each electrode is 1 cm × 1 cm, and the weight of each electrode is about 2 mg. The density of the electrodes was estimated to be 0.2 g cm^{-3}. We also used conventional process to make electrodes by mixing CuO nanobelts with carbon black and the PVDF binder (9:1:1 weight ratio), which was named as CuO/CB electrode. Flexible electrodes were also fabricated by depositing CuO/CNT network films (100 μm thick) onto SWCNT films (50 μm thick). In a typical method, SWCNTs in ethanol solution was added to a Teflon box. And then the CuO nanobelts and SWCNTs (9:1 weight ratio) in ethanol solution were added to the box when the SWCNT solution dried. The electrochemical performance of the electrodes was evaluated on a CHI 660B workstation and Solartron analytical equipment (model 1470E) for CV, EIS, and chronopotentiometry (CP) tests by using a three-electrode cell with Pt foil as the counter electrode and a saturated calomel electrode (SCE) as the reference electrode.

Acknowledgment. The authors gratefully acknowledge the AcRF Tier 1 RG 31/08 from MOE Singapore and NRF2009EWT-CERP001-026 Singapore, Singapore Ministry of Education (MOE2010-T2-1-017), the National Natural Science Foundation of China (Nos. 20901003 and 21073001) and the Young Teacher Program of Anhui Normal University (2009xqnzc19).

Supporting Information Available: Details of process of porous CuO nanobelts, XRD, BET, and SEM images of the surface of defferent electrodes. This material is available free of charge *via* the Internet at http://pubs.acs.org.

REFERENCES AND NOTES

1. Subramanian, V.; Zhu, H.; Vajtai, R.; Ajayan, P. M.; Wei, B. Hydrothermal Synthesis and Pseudocapacitance Properties of MnO_2 Nanostructures. *J. Phys. Chem. B* **2005,** *109*, 20207–20214.
2. Mohana, A. L.; Estaline, R. F.; Imran, A.; Ramaprabhu, J. S. Asymmetric Flexible Supercapacitor Stack. *Nanoscale Res. Lett.* **2008,** *3*, 145–151.
3. A. Karina, C. G.; Monica, L. C.; Nieves, C. P.; Pedro, G. R. Nanocomposites Hybrid Molecular Materials for Application in Solid-State Electrochemical Supercapacitors. *Adv. Funct. Mater.* **2005,** *15*, 1125–1133.
4. Brezesinski, T.; Wang, J.; Tolbert, S. H.; Dunn, B. Ordered Mesoporous α-MoO_3 with Iso-oriented Nanocrystalline Walls for Thin-Film Pseudocapacitors. *Nat. Mater.* **2010,** *9*, 146–151.
5. Hou, Y.; Cheng, Y. W.; Hobson, T.; Liu, J. Design and Synthesis of Hierarchical MnO_2 Nanospheres/Carbon Nanotubes/Conducting Polymer Ternary Composite for High Performance Electrochemical Electrodes. *Nano Lett.* **2010,** *10*, 2727–2733.

6. Reddy, A. L. M.; Shaijumon, M. M.; Gowda, S. R.; Ajayan, P. M. Multisegmented Au-MnO_2/Carbon Nanotube Hybrid Coaxial Arrays for High-Power Supercapacitor Applications. *J. Phys. Chem. C* **2010,** *114*, 658–663.
7. Shim, Y. S.; Kim, H. J. Nanoporous Carbon Supercapacitors in an Ionic Liquid: A Computer Simulation Study. *ACS Nano* **2010,** *4*, 2345–2355.
8. Sassin, M. B.; Mansour, A. N.; Pettigrew, K. A.; Rolison, D. R.; Long, J. W. Electroless Deposition of Conformal Nanoscale Iron Oxide on Carbon Nanoarchitectures for Electrochemical Charge Storage. *ACS Nano* **2010,** *4*, 4505–4514.
9. Lee, S. W.; Kim, J. Y.; Chen, S.; Hammond, P. T.; Horn, Y. S. Carbon Nanotube/Manganese Oxide Ultrathin Film Electrodes for Electrochemical Capacitors. *ACS Nano* **2010,** *4*, 3889–3896.
10. Balasubramanian, B.; Kraemer, K. L.; Reding, N. A.; Skomski, R.; Ducharme, S.; Sellmyer, D. J. Synthesis of Monodisperse TiO_2 Paraffin Core Shell Nanoparticles for Improved Dielectric Properties. *ACS Nano* **2010,** *4*, 1893–1900.
11. Zhang, J. T.; Ma, J. Z.; Zhang, L. L.; Guo, P. Z.; Jiang, J. W.; Zhao, X. S. Template Synthesis of Tubular Ruthenium Oxides for Supercapacitor Applications. *J. Phys. Chem. C* **2010,** *114*, 13608–13613.
12. Chang, K. H.; Hu, C. C.; Chou, C. Y. Textural and Capacitive Characteristics of Hydrothermally Derived $RuO_2 \cdot xH_2O$ Nanocrystallites: Independent Control of Crystal Size and Water Content. *Chem. Mater.* **2007,** *19*, 2112–2119.
13. Hu, C. C.; Chang, K. H.; Lin, M. C.; Wu, Y. T. Design and Tailoring of the Nanotubular Arrayed Architecture of Hydrous RuO_2 for Next Generation Supercapacitors. *Nano Lett.* **2006,** *6*, 2690–2695.
14. Son, J. Y.; Shin, Y. H.; Kim, H. J.; Jang, H. M. NiO Resistive Random Access Memory Nanocapacitor Array on Graphene. *ACS Nano* **2010,** *4*, 2655–2658.
15. Hosogai, S.; Tsutsumi, H. Electrospun Nickel Oxide/Polymer Fibrous Electrodes for Electrochemical Capacitors and Effect of Heat Treatment Process on Their Performance. *J. Power Sources* **2009,** *194*, 1213–1217.
16. Gupta, V.; Gupta, S.; Miura, N. Electrochemically Synthesized Large Area Network of $Co_xNi_yAl_z$ Layered Triple Hydroxides Nanosheets: A High Performance Supercapacitor. *J. Power Sources* **2009,** *189*, 1292–1295.
17. Srinivasan, V.; Weidner, J. W. Capacitance Studies of Cobalt Oxide Films Formed *via* Electrochemical Precipitation. *J. Power Sources* **2002,** *108*, 15–20.
18. Zou, W. Y.; Wang, W.; He, B. L.; Sun, M. L.; Yin, Y. S. Supercapacitive Properties of Hybrid Films of Manganese Dioxide and Polyaniline Based on Active Carbon in Organic Electrolyte. *J. Power Sources* **2010,** *195*, 7489–7493.
19. Xu, C. L.; Zhao, Y. Q.; Yang, G. W.; Lia, F. S.; Li, H. L. Mesoporous Nanowire Array Architecture of Manganese Dioxide for Electrochemical Capacitor Applications. *Chem. Commun.* **2009,** 7575–7577.
20. Long, J. W.; Sassin, M. B.; Fischer, A. E.; Rolison, D. R. Multifunctional MnO_2-Carbon Nanoarchitectures Exhibit Battery and Capacitor Characteristics in Alkaline Electrolytes. *J. Phys. Chem. C* **2009,** *113*, 17595–17598.
21. Qu, Q. T.; Shi, Y.; Li, L. L.; Guo, W. L.; Wu, Y. P.; Zhang, H. P.; Guan, S. Y.; Holze, R. V_2O_5_0.6H_2O Nanoribbons as Cathode Material for Asymmetric Supercapacitor in K_2SO_4 Solution. *Electrochem. Commun.* **2009,** *11*, 1325–1328.
22. Nam, K. W.; Ma, S. B.; Yoon, W. S.; Yang, X. Q.; Kim, K. B. Novel Concept of Pseudocapacitor Using Stabilized Lithium Metal Powder and Nonlithiated Metal Oxide Electrodes in Organic Electrolyte. *Electrochem. Commun.* **2009,** *11*, 1166–1169.
23. Wang, H. L.; Cui, L. F.; Yang, Y.; Casalongue, H. S.; Robinson, O. T.; Liang, Y. Y.; Cui, Y.; Dai, H. J. Mn_3O_4-Graphene Hybrid as a High-Capacity Anode Material for Lithium Ion Batteries. *J. Am. Chem. Soc.* **2010,** *132*, 13978–13980.
24. Cain, M. F.; Hughes, R. P.; Glueck, D. S.; Golen, J. A.; Moore, C. E.; Rheingold, A. L. Synthesis and Structure of Intermediates in Copper-Catalyzed Alkylation of Diphenylphosphine. *Inorg. Chem.* **2010,** *49*, 7650–7662.
25. Bedi, R. K.; Singh, I. Room-Temperature Ammonia Sensor Based on Cationic Surfactant-Assisted Nanocrystalline CuO. *ACS Appl. Mater. Interfaces* **2010,** *2*, 1361–1368.
26. Hoa, N. D.; Quy, N. V.; Jung, H.; Kim, D.; Kim, H.; Hong, S. K. Synthesis of Porous CuO Nanowires and Its Application to Hydrogen Detection. *Sens. Actuators B* **2010,** *146*, 266–272.
27. Park, J. C.; Kim, J.; Kwon, H.; Song, H. Gram-Scale Synthesis of Cu_2O Nanocubes and Subsequent Oxidation to CuO Hollow Nanostructures for Lithium-Ion Battery Anode Materials. *Adv. Mater.* **2009,** *21*, 803–807.
28. Dubal, D. P.; Dhawale, D. S.; Salunkhe, R. R.; Jamdade, V. S.; Lokhande, C. D. Fabrication of Copper Oxide Multilayer Nanosheets for Supercapacitor Application. *J. Alloys Compd.* **2010,** *492*, 26–30.
29. Patakea, V. D.; Joshi, S. S.; Lokhande, C. D.; Joo, O. S. Electrodeposited Porous and Amorphous Copper Oxide Film for Application in Supercapacitor. *Mater. Chem. Phys.* **2009,** *114*, 6–9.
30. Du, G. H.; Tendeloo, G. V. $Cu(OH)_2$ Nanowires, CuO Nanowires, and CuO Nanobelts. *Chem. Phys. Lett.* **2004,** *393*, 64–69.
31. Xiang, J. Y.; Tu, J. P.; Zhang, J.; Zhong, J.; Zhang, D.; Cheng, J. P. Incorporation of MWCNTs into Leaf-like CuO Nanoplates for Superior Reversible Li-Ion Storage. *Electrochem. Commun.* **2010,** *12*, 1103–1107.
32. Venkatachalam, S.; Zhu, H. W.; Masarapu, C.; Hung, K. H.; Liu, Z.; Suenaga, K.; Wei, B. Q. *In-Situ* Formation of Sandwiched Structures of Nanotube/Cu_xO_y/Cu Composites for Lithium Battery Applications. *ACS Nano* **2009,** *3*, 2177–2184.
33. Kaempgen, M.; Chan, C. K.; Ma, J.; Cui, Y.; Gruner, G. Printable Thin Film Supercapacitors Using Single-Walled Carbon Nanotubes. *Nano Lett.* **2009,** *9*, 1872–1876.
34. Ban, C. M.; Wu, Z. C.; Gillaspie, D. T.; Chen, L.; Yan, Y. F.; Blackburn, J. L.; Dillon, A. C. Nanostructured Fe_3O_4/SWNT Electrode: Binder-free and High-Rate Li-Ion Anode. *Adv. Mater.* **2010,** *22*, 145–149.
35. Yuan, C. Z.; Zhang, X. G.; Su, L. H.; Gao, B.; Shen, L. F. Facile Fynthesis and Self-Assembly of Hierarchical Porous NiO Nano/Micro Spherical Superstructures for High Performance Supercapacitors. *J. Mater. Chem.* **2009,** *19*, 5772–5777.
36. Jurewicz, K.; Frackowiak, E.; Be'guin, F. Towards the Mechanism of Electrochemical Hydrogen Storage in Nanostructured Carbon Materials. *Appl. Phys. A: Mater. Sci. Process* **2004,** *78*, 981–987.
37. Chen, Z.; Qin, Y. C.; Weng, D.; Xiao, Q. F.; Peng, Y. T.; Wang, X. L.; Li, H. X.; Wei, F.; Lu, Y. F. Design and Synthesis of Hierarchical Nanowire Composites for Electrochemical Energy Storage. *Adv. Funct. Mater.* **2009,** *19*, 3420–3426.
38. Simon, P.; Gogotsi, Y. Materials for Electrochemical Supercapacitor. *Nat. Mater.* **2008,** *7*, 845–854.
39. Wang, D. W.; Li, F.; Liu, M.; Lu, G. Q.; Cheng, H. M. 3D Aperiodic Hierarchical Porous Graphitic Carbon Material for High-Rate Electrochemical Capacitive Energy Storage. *Angew. Chem., Int. Ed.* **2008,** *47*, 373–376.
40. Yan, J.; Fan, Z. J.; Wei, T.; Cheng, J.; Shao, B.; Wang, K.; Song, L. P.; Zhang, M. L. Carbon Nanotube/MnO_2 Composites Synthesized by Microwave-Assisted Method for Supercapacitors with High Power and Energy Densities. *J. Power Sources* **2009,** *194*, 1202–1207.
41. Yan, J.; Khoo, E.; Sumboja, A.; Lee, P. S. Facile Coating of Manganese Oxide on Tin Oxide Nanowires with High-Performance Capacitive Behavior. *ACS Nano* **2010,** *4*, 4247–4255.
42. Kaempgen, M.; Chan, C. K.; Ma, J.; Cui, Y; Gruner, G. Printable Thin Film Supercapacitors Using Single-Walled Carbon Nanotubes. *Nano Lett.* **2009,** *9*, 1872–1876.